Received: 12 May 2020 | Revised: 4 September 2020 | Accepted: 12 October 2020

DOI: 10.1002/aic.17111

TRANSPORT PHENOMENA AND FLUID MECHANICS

AIChE JOURNAL

Micro-computed tomography for the 3D time-resolved investigation of monodisperse droplet generation in a co-flow setup

Julia Schuler | Laura Maria Neuendorf | Kai Petersen | Norbert Kockmann

Laboratory of Equipment Design, Department of Biochemical and Chemical Engineering, TU Dortmund University, Dortmund, Germany

Correspondence
Julia Schuler, Laboratory of Equipment Design, Department of Biochemical and Chemical Engineering, TU Dortmund University, 44227 Dortmund, Germany.
Email: julia.schuler@tu-dortmund.de

Funding information
Deutsche Forschungsgemeinschaft, Grant/Award Number: INST 212/397-1

Abstract

Droplet generation in microfluidic devices has emerged as a promising approach for the design of highly controllable processes in the chemical and pharmaceutical industry. However, droplet generation is still not fully understood due to the complexity of the underlying physics. In this work, micro-computed tomography is applied to investigate droplet formation in a circular channel in a co-flow configuration at different flow conditions (Ca < 0.001). The application of an in-house developed scanning protocol assisted by comprehensive image processing allows for the time-resolved investigation of droplet formation. By tracking different droplet parameters (length, radii, volume, surface, Laplace pressure) the effect of flow conditions on droplet progression is determined. As characteristic for the squeezing regime, final droplet size was nearly independent of Ca for higher Ca tested. For lower Ca, the final droplet size increased with decreasing Ca, which points to the leaking regime that was recently introduced in the literature.

KEYWORDS
co-flow, droplet generation, image processing, micro-computed tomography, microfluidics

1 | INTRODUCTION

Process intensification via miniaturization has proven to be a suitable approach to design safe, sustainable processes in the chemical and pharmaceutical industry due to high surface to volume ratios, short diffusion lengths, and excellent mixing behavior. Furthermore, strictly laminar flows make processes tunable and controllable. Within the wide field of micro process engineering, segregated flows in small channels, such as bubble, droplet, and slug flow, have emerged as a major approach. The application of droplet flow includes, among others, the synthesis of chemicals and materials,[1-5] kinetic studies,[6,7] solvent extraction,[8,9] protein crystallization,[10,11] drug discovery[12,13] and delivery,[14] and cell culture.[13]

Due to the wide range of applications of droplet flow and bubble flow in miniaturized equipment also droplet generators and channel geometry vary according to the application. Common droplet generation approaches are cross-flow,[15] as the T-junction,[16-21] where the continuous phase and dispersed phase meet perpendicularly, flow-focusing,[22-25] where the dispersed phase is elongated by shear forces imposed by the continuous phase, and the co-flow configuration,[26-29] where the dispersed phase is introduced to the continuous phase with a thin needle that intrudes into the main channel concentrically. Most microfluidic devices consist of rectangular channels, however, circular[30-34] or even trapezoidal[35,36] cross-sections are possible, too. Despite the variety of geometric configurations, similar break-up mechanisms can be found for different geometric configurations.[37] In microfluidics, Reynolds number is generally low such that the resulting flow is strictly laminar.[37] Important parameters that affect the droplet formation and break-up in confined geometries are the capillary

number Ca, flow rate ratio ϕ, and the generator geometry.[19,37-39] In Equation (1) $\dot{V}_{dis}$ and $\dot{V}_c$ are the volume flow rates of the dispersed (index dis) and the continuous phase (index c). The capillary number, Equation (2), depends on dynamic viscosity η_c, the mean velocity of the continuous phase v_c, and interfacial tension γ.

$$\phi = \frac{\dot{V}_{dis}}{\dot{V}_c} \tag{1}$$

$$\mathrm{Ca} = \frac{\eta_c v_c}{\gamma} \tag{2}$$

Depending on flow conditions, different regimes are distinguished. For low Ca (Ca < 0.01) interfacial stresses dominate viscous stresses and droplet formation takes place in the pressure dominated squeezing regime.[17,20,21,37,40] For higher Ca, viscous forces gain in importance and lead to droplet break-up according to the dripping or jetting regime.[17,37,38] The squeezing regime is divided into different stages. In the first stage, called the filling stage, the droplet begins to grow into the main channel and the continuous phase can bypass the droplet easily, see Figure 1(a). At the end of the filling stage, the droplet obstructs the main channel completely, except for a thin film between the droplet and the channel wall. In the second stage, the necking stage, the continuous fluid can no longer bypass the droplet as easily due to the high flow resistance imposed by the small gap between droplet and channel wall. This causes the upstream pressure in the continuous phase to rise and leads to the formation of a neck, see Figure 1(b).[17,21,38,40] As more continuous phase is pushed towards the emerging droplet the radius of the neck decreases until the droplet pinches off due to a Rayleigh-Plateau like instability.[23]

Findings from the investigation of the mechanisms in the squeezing regime have led to different scaling laws for the prediction of the resulting droplet size, depending on flow conditions and geometry. Garstecki et al.[17] proposed a simple and widely accepted scaling law for the prediction of the resulting droplet length $l_{d,det}$ in rectangular channels with width w_c, see Equation (3). The scaling law states that the resulting dimensionless droplet length solely depends on the flow rate ratio ϕ and a geometry dependent factor α, which has to be fitted to experiments.[21]

$$l_{d,det}/w_c = 1 + \alpha \cdot \phi \tag{3}$$

Even in the necking stage, a non-negligible portion of the continuous phase bypasses the emerging droplet/bubble.[41,42,40] Recently, Korczyk et al.[18] published a mathematical model taking into account the flow around the droplet in the necking stage. In the model, the flow rate of the continuous phase is divided into a proportion bypassing the emerging droplet $\dot{V}_b$ and a proportion contributing to the necking of the droplet $\dot{V}_n$. $\dot{V}_b$ can be obtained from the pressure balance in Equation (4), where the flow resistance R_b depends on the length of the emerging droplet.[18]

$$\gamma(K_F - K_B) = R_b \dot{V}_b \tag{4}$$

The curvature at the front of the droplet K_F is assumed to remain constant whereas the curvature at the rear end of the droplet K_B is affected by $\dot{V}_n$. Equation (4) is modeled through the electric hydraulic analogy, which results in the model presented in Equation (5).[18] The authors extended the classic understanding of droplet formation by a new regime, the leaking regime, where the resulting droplet length

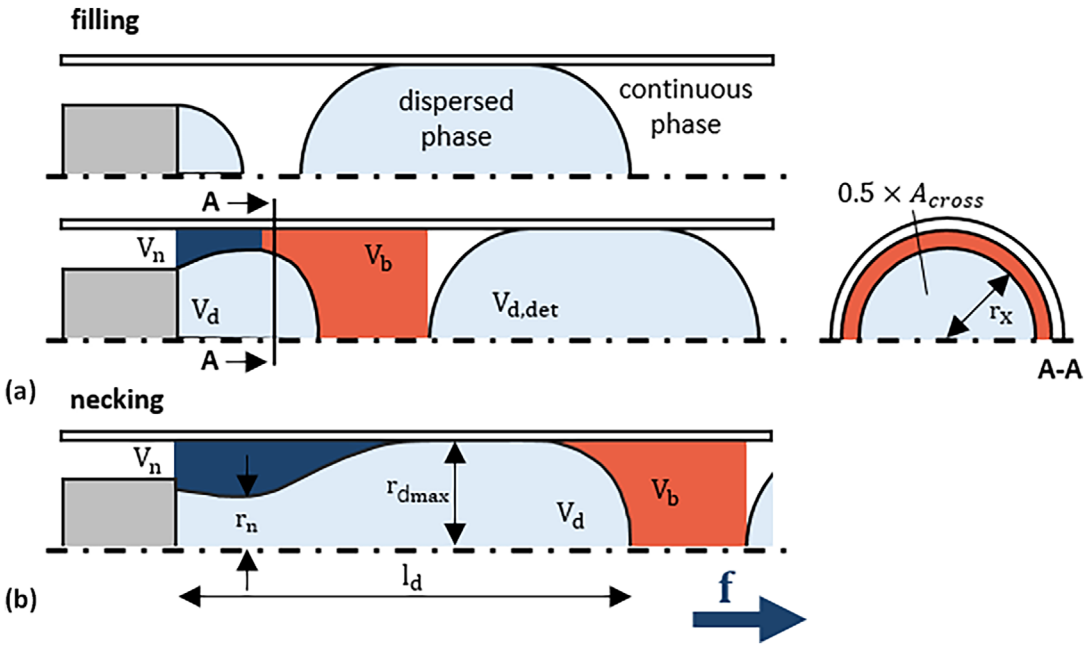

FIGURE 1 Evolution of the droplet shape during droplet formation in a co-flow configuration with tracked properties of the continuous phase (white) and thedispersedphase (light blue). (a) filling stage (b) necking stage. The blue arrow f indicates the flow direction [Color figure can be viewed at wileyonlinelibrary.com]

strongly depends on the capillary number Ca for very low Ca.[18] In Equation (5) $l^*_{d,det}$, l^*_{fill}, and ν^*_{fill} are the dimensionless droplet length after droplet detachment, at the end of the filling stage, and the dimensionless droplet volume gained in the filling stage.[18] β is a geometry dependent coefficient.[18]

$$l^*_{d,det} = l^*_{fill} + \phi\,\nu^*_{fill}\left(1 + \frac{\beta}{\phi\,Ca}\right) \tag{5}$$

A detailed investigation of droplet formation includes the consideration of the three-dimensionality of the process. By applying microparticle image velocimetry (μ-PIV) van Steijn et al.[40] demonstrated that 3D flow in the corners of rectangular channels plays an important role in droplet break-up. Additionally, the importance of the 3D interface of droplets has already been recognized.[37] However, despite the great achievements in physical understanding of droplet formation and predicting droplet size in the squeezing regime in the past decades, the role of the three-dimensionality of droplet formation has not been cleared sufficiently. Three-dimensional droplet quantities are mostly derived from 2D photographs, applying theoretical methods,[43] as a noninvasive 3D imaging approach is missing.

In this work, we tie in with this research gap and apply X-ray based micro-computed tomography (µ-CT) for the investigation of droplet formation in circular capillaries. X-ray based µ-CT is a noninvasive measurement technique allowing high spatial resolutions (<10 µm) and overcoming the challenges related to optical imaging.[44] Despite the wide use of tomographic imaging in the fields of chemical engineering and process engineering,[45-51] the extension to mini- and microfluidics is an innovative approach.[44] One major challenge in using X-ray based tomographic imaging for dynamic processes in micro process engineering is the limited temporal resolution, which can range from a few minutes to several hours. In this work, this is met by the application of an in-house developed scanning protocol and postprocessing routine, called the multiple-select method, for time-resolved 3D imaging of periodic droplet generation. Hence, temporal resolution is enhanced significantly (≈ 0.05 s). This allows for the tracking of different 3D droplet quantities, such as volume and surface, over time.

2 | METHODS AND MATERIALS

2.1 | Experimental setup

Water droplets are generated in silicone oil using a co-flow configuration, as shown in Figure 2(b). A polymer cannula (polyurethane, d_i = 800 µm, d_o = 1100 µm) is inserted into a polymer tube (fluorinated ethylene propylene (FEP), $d_i \approx$ 1580 µm). The cannula is fixed with a T-junction, which allows introducing the dispersed phase (index dis) through the bottom inlet and the continuous phase (index c) through the side inlet. Here, the outlet of the cannula is not centered inside the tube but is inclined to the tube wall, such that the set-up is not axisymmetrical. The asymmetry of the set-up can be expressed in

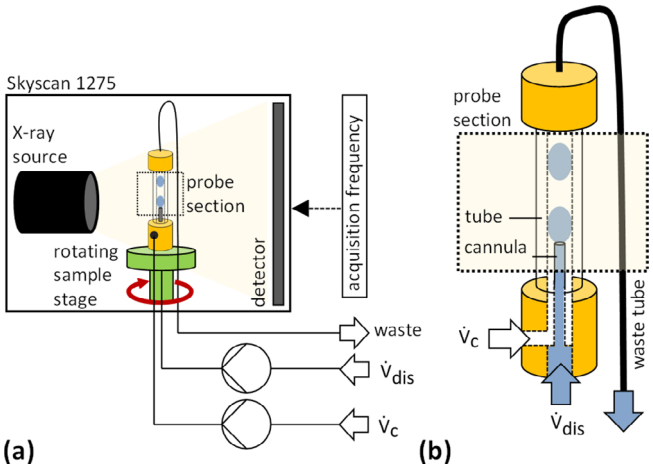

FIGURE 2 Schematic of the experimental setup. (a) Overview of experimental setup mounted into the Skyscan 1275. (b) Schematic of the droplet generation device in the co-flow configuration [Color figure can be viewed at wileyonlinelibrary.com]

terms of the distance between the center of the cannula and the center of the tube at the height of the cannula outlet and is in the range of 0.23 mm (run O) and 0.13 mm (run R). X-ray projection images are acquired in the Bruker Skyscan 1275 µ-CT scanner (RJL Micro & Analytic GmbH, Karlsdorf Neuthart, Germany). The flow generator is mounted onto the sample stage that is placed between the X-ray source (100 W, 20 kV-100 kV) and the distortion-free 3Mp flat panel detector (1,944 x 1,536 pixels),[52] see Figure 2(a). The spatial resolution obtained with this setup is 12 µm. For tomographic imaging, a set of projection images from different angular positions, covering a range of at least 180°, is required to enable reconstruction to 3D data. This can be realized by using multiple scanners that acquire projection images at different angular positions simultaneously. However, in this work another approach is chosen that can be easily applied in a commercially available CT scanner. Thereby, the sample stage is rotated by 0.25° after the acquisition of each projection image until a range of 224° is covered. Pumps for water (BlueShadow Pump 40P, KNAUER Wissenschaftliche Geräte GmbH, Berlin, Germany) and silicone oil (Syrdos Precision Syringe Dosing Device, HiTec Zang GmbH, Herzogenrath Germany) are placed outside the µ-CT scanner and connected to the droplet generator via FEP-tubes. The pumps were calibrated before the experiment and the total adjusted flow rate was measured multiple times gravimetrically during each experiment to eliminate errors.

In each experiment, the flow of the continuous phase is started before the flow of the dispersed phase to ensure complete wetting of the inner tube wall for all experiments. Additionally, silicone oil and water are equilibrated for >24 h before the experiment. To test the effect of viscosity of the continuous phase on droplet generation different silicone oils (PDMS-1cSt, PDMS-5cSt, PDMS-10cSt, *ELBESIL-Öle B, L. Böwing GmbH, Hofheim, Germany)* are used. Flow rate ratio $\phi = \dot{V}_{dis}/\dot{V}_c$ is varied between 0.667 and 1.5 with a total volume flow rate held constant at 0.5 mL min^{-1}. The experimental conditions are summarized in Table 1. Experiments are conducted twice to ensure

Oil ID	ϕ	Range of Ca number	Range of Re number
PDMS-1cSt	1.5 / 1 / 0.667	4.7×10^{-5} – 7.0×10^{-5}	2.3–3.4
PDMS-5cSt	1.5 / 1 / 0.667	2.5×10^{-5} - 3.8×10^{-4}	0.5–0.8
PDMS-10cSt	1.5 / 1 / 0.667	5.7×10^{-4} - 8.6×10^{-4}	0.3–0.4

TABLE 1 Overview of experiments conducted in this work. Experiments are conducted with different silicone oils (oil ID) as the continuous phase and deionized water as the dispersed phase

TABLE 2 Properties of silicone oils used as the continuous phase. The interfacial tension γ is measured against deionized water. Measurements are carried out at ambient conditions (T_a = 21.5 ± 1 C)

Oil ID	η_c / mPas	γ / mNm	ρ_c / kg m^{-3}
PDMS-1cSt	0.96	34.7	814.8
PDMS-5cSt	4.50	30	901.6
PDMS-10cSt	9.37	27.7	923.9

reproducibility. Between the experimental runs it was necessary to update the flat field correction. The flatfield correction calibrates the background image and must be updated regularly to avoid poor imaging results. However, dismounting and reinstallation of the droplet generator were necessary to update the flat field correction. Therefore, the configuration of the two different experimental runs (inclination of the whole setup, the relative position between cannula and tube) varies slightly. Consequently, the different experimental runs are marked with O (original run) and R (reproduction run).

Properties of the silicone oils are measured before the experiments using a tensiometer (K10ST, A.KRÜSS Optronic GmbH, Hamburg, Germany) for the determination of the surface tension and a rotational viscometer (HAAKE MARS 60 Rheometer, Thermo Fisher Scientific Inc., Waltham, MA USA) for the determination of viscosity (Table 2). These experiments are done in triplets to ensure reproducibility.

2.2 | Scanning protocol and postprocessing

Originally, the temporal resolution of tomographic imaging is low as a whole set of projection images is required for the reconstruction of 2D projections to a 3D data set. This limits the application of computed tomography to static or very slow problems. Movement of the sample is highly undesirable as it leads to perturbations in the resulting 3D images, called movement artifacts. In this work, we present a methodology to make tomographic imaging applicable to the investigation of droplet generation in the squeezing and leaking regime. Droplet generation is highly reproducible in these stages. Therefore, the droplet undergoes the same states during droplet formation again and again. Hereby, we define a droplet state as a certain length that the droplet has during its generation process. This is used for the so-called multiple-select method that is based on the postacquisition synchronization approach, which is also utilized in biomedical imaging.[53-55] The multiple-select method for the time-resolved imaging of droplet generation is depicted in Figure 3(a) schematically. For each angular position, 65 X-ray projections are acquired at a frequency of $f \approx$ 5.45 Hz (1). This should result in a set of 65 projection images per angular position, each showing the droplet with a different length, hence in a different state. Conversely, for a given droplet length l_d one X-ray projection showing the droplet approximately in the defined stage (length l_d) should exist in every set of 65 projection images. Therefore, the second step of the multiple-select method (2) consists of the selection of one out of 65 X-ray projections that represents best the droplet with the defined length l_d for every angular position. This results in a data set showing the droplet with approximately the same length for every angular position (3). This data set is reconstructed to a 3D data set using commercially available reconstruction software NRecon (Bruker, Billerica, MA) (4). By repeating this for different droplet lengths l_d time-resolved CT data is obtained.

For the selection of the appropriate projection for each angular position (step (2)), the projections are segmented using a pretrained convolutional neural network (CNN), the vgg16 net.[56] The vgg16 is chosen as it is a good compromise between accuracy and computation speed.[57] It consists of 16 weight layers and applies small convolutional filters (3 x 3).[56] The vgg16 net is pretrained with the ILSVRC-2012 dataset, 1.3 M training images respectively, and was the winner of the ImageNet Challenge 2014.[56] It was adjusted to the segmentation of droplets by training it with own training data in MATLAB. Original training data consist of 180 X-ray projection images and photographs showing droplets during droplet generation in the co-flow configuration. This data set was artificially enlarged in MATLAB by scaling, rotating, shearing, mirroring, and translating the original data set, which results in a larger final training set. The net proofed to be robust and accurate when testing on validation data. In test projection images, 97% of the pixels were assigned to either water, oil, cannula, tube, or background correctly. After segmentation, droplet lengths could be easily determined by applying the built-in MATLAB function *regionprops*. Figure 3(b) exemplarily shows a segmentation result for one X-ray projection with droplet length l_d found by *regionprops*.

The reconstructed data sets consist of gray-value voxels, the 3D equivalent of pixels, see Figure 3(c). These voxels need to be assigned to either water, oil, cannula, tube, or background according to their gray values. The segmentation is, again, done with a pretrained vgg16 net, that was adjusted to the segmentation task by training in MATLAB in the same manner as described before.

In this work, different droplet quantities are tracked, see Figure 1. These quantities can be divided into volumes, surfaces, and lengths/diameters. Volumes are obtained by summing voxels assigned to the desired phase and multiplying with (isotropic edge length = 12 μm)^3.

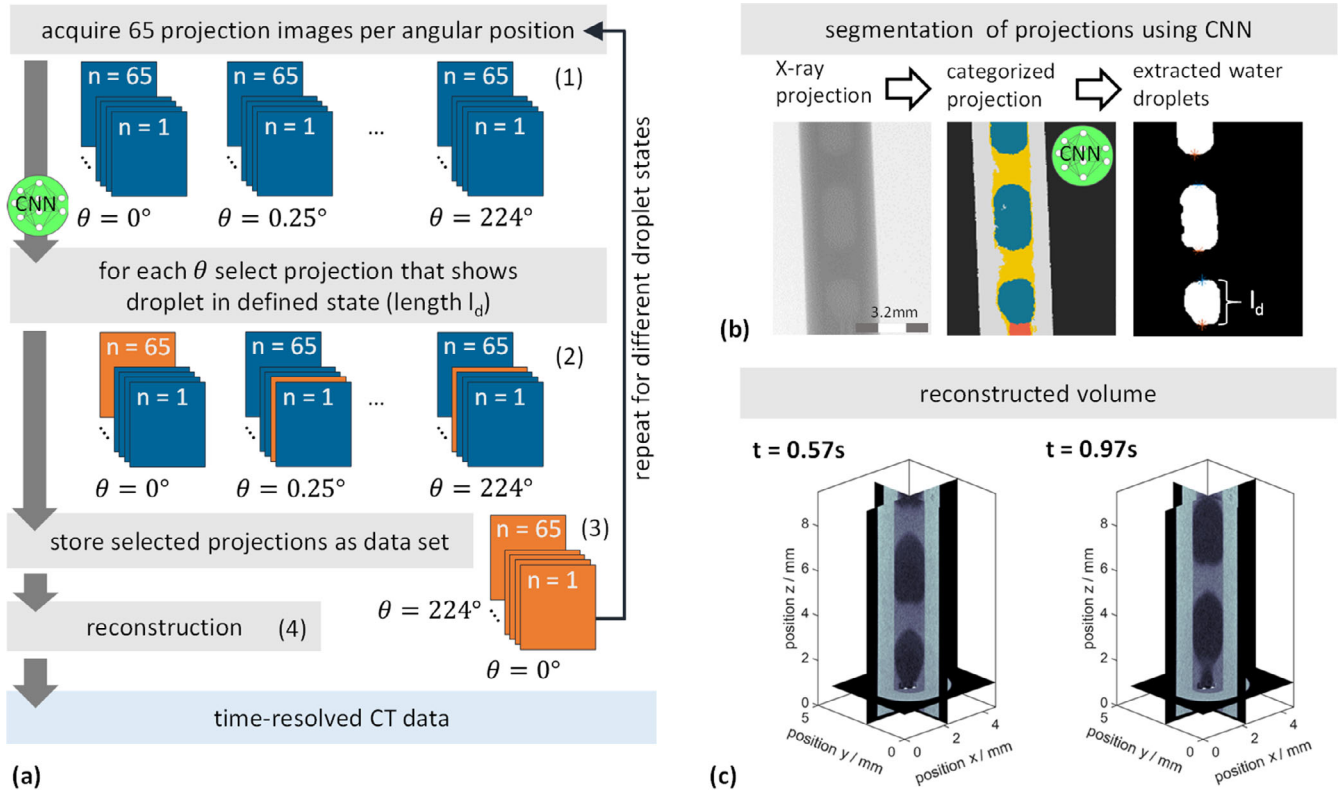

FIGURE 3 (a) Principle of the multiple-select method. Multiple projection images (1) are acquired at each angular position (range 0°–224°). For each angular position, one projection image is selected that represents best the desired droplet state (2), defined by the droplet length l_d. The final projection set (3) is reconstructed to a 3D volume (4). (b) Segmentation of X-ray projections using CNN and extraction of droplet length. (c) Visualization of reconstructed data (configuration O,ϕ = 1.5, PDMS-1cSt) [Color figure can be viewed at wileyonlinelibrary.com]

The local droplet radii r_x are calculated using the cross-sectional area A_{cross} (see Figure 1(a)) at discrete positions in flow direction according to Equation (6). The concrete value of A_{cross} at each discrete position is obtained by summing all voxels that are assigned to the dispersed phase at the discrete position and multiplying with (isotropic edge length = 12 μm)^2.

$$d_x = \sqrt{A_{cross} \cdot \frac{4}{\pi}} \tag{6}$$

For the calculation of the PDMS/water surface area, the droplet is approximated as a stack of truncated cones with a height of 12 μm (spatial resolution), whose shell surfaces can be calculated easily. The diameters of the truncated cones are the diameters of two neighboring cross-sections with area A_{cross}.

3 | RESULTS AND DISCUSSION

3.1 | Analysis of droplet generation

3D representations of the forming droplets for three different experimental conditions (Ca, ϕ) are given in Figure 4. For each flow condition, the droplet is shown at the beginning of the formation cycle (t = 0 s), at $t \approx 0.8$ s and shortly before pinch-off. For Ca = $7 \cdot 10^{-5}$ and $\phi = 0.67$ (middle), the droplet slowly grows in flow direction until it pinches off after $t \approx 1.17$ s. As expected for a low flow rate ratio ϕ, the resulting droplet is relatively small but droplet spacing is large. For higher ϕ (bottom row in Figure 4), the resulting droplets are larger and droplet spacing is shorter, as already reported in the literature.[17,37,39] Additionally, the droplet evolves faster. At $t \approx 0.8$ s, the droplet is not only larger but also pushed further into downstream direction for $\phi = 1.5$ than for $\phi = 0.67$, which results in a smaller neck radius at the same time. This leads to a shorter formation cycle for higher ϕ as the droplet is expected to pinch-off when a critical minimum neck

radius is reached.[20,21,38,40] For $\phi = 0.67$ and Ca = $8.6 \cdot 10^{-4}$ (top row in Figure 4), the resulting droplet volume is smaller compared to the droplet resulting from $\phi = 0.67$ and Ca = $7 \cdot 10^{-5}$

(middle row in Figure 4). As can be seen from the figure, the droplet evolves a little more in flow direction than in radial direction. At $t \approx 0.8$ s the droplet in the top row of Figure 4 (high Ca) is pushed further in the downstream direction than the droplet in the middle row of Figure 4 (lower Ca) although the droplet has not reached its maximum radial extension yet. This leads to earlier pinch-off, which explains the smaller resulting volume for higher Ca. The qualitatively observed dependency between capillary number and final droplet volume supports the existence of a leaking regime.[18]

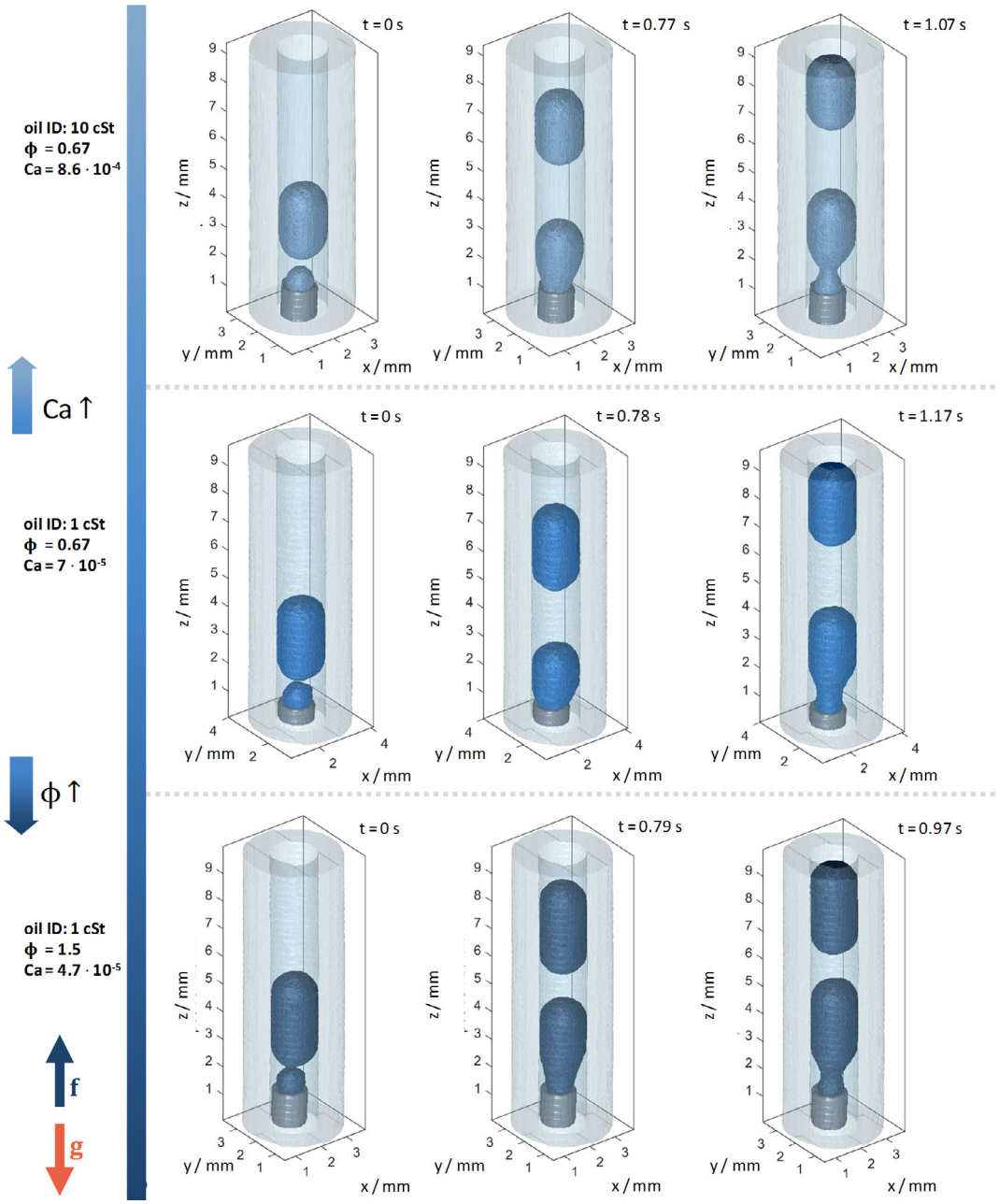

FIGURE 4 3D representation of the evolution of droplets for different flow conditions in the O-configuration. Shown is the qualitative dependence of droplet evolution on Ca andϕ. Flow direction is marked with f and direction of gravity is marked with g [Color figure can be viewed at wileyonlinelibrary.com]

Figure 4 gives an excellent qualitative impression of how droplets evolve under different circumstances. For a deeper understanding of droplet evolution in the filling and necking stage, different droplet quantities are discussed in the following sections.

3.2 | Evolution of droplet parameters over time

Figure 5(a)–(f) show the evolution of different droplet quantities for the different experimental conditions over time. Figure 5(a) shows the volume of the emerging water droplet $V_d(t)$. As can be seen in the figure, droplets have positive volumes at $t = 0\,s$ for all experimental conditions, which means that the droplet interface does not retract into the cannula after pinch-off. Then, the volume increases linearly over time. The flow rates calculated from the slopes of each curve approximate the volume flow rates of water that were adjusted at the pump (0.2 mL min^{-1}, 0.25 mL min^{-1}, 0.3 mL min^{-1}) with an average error < 2.7%.

The remaining droplet parameters that are shown in Figure 5(b)–(f) are considered separately for the filling stage and the necking stage. The transition between the filling stage and the necking stage happens at different times for different flow conditions, as will be

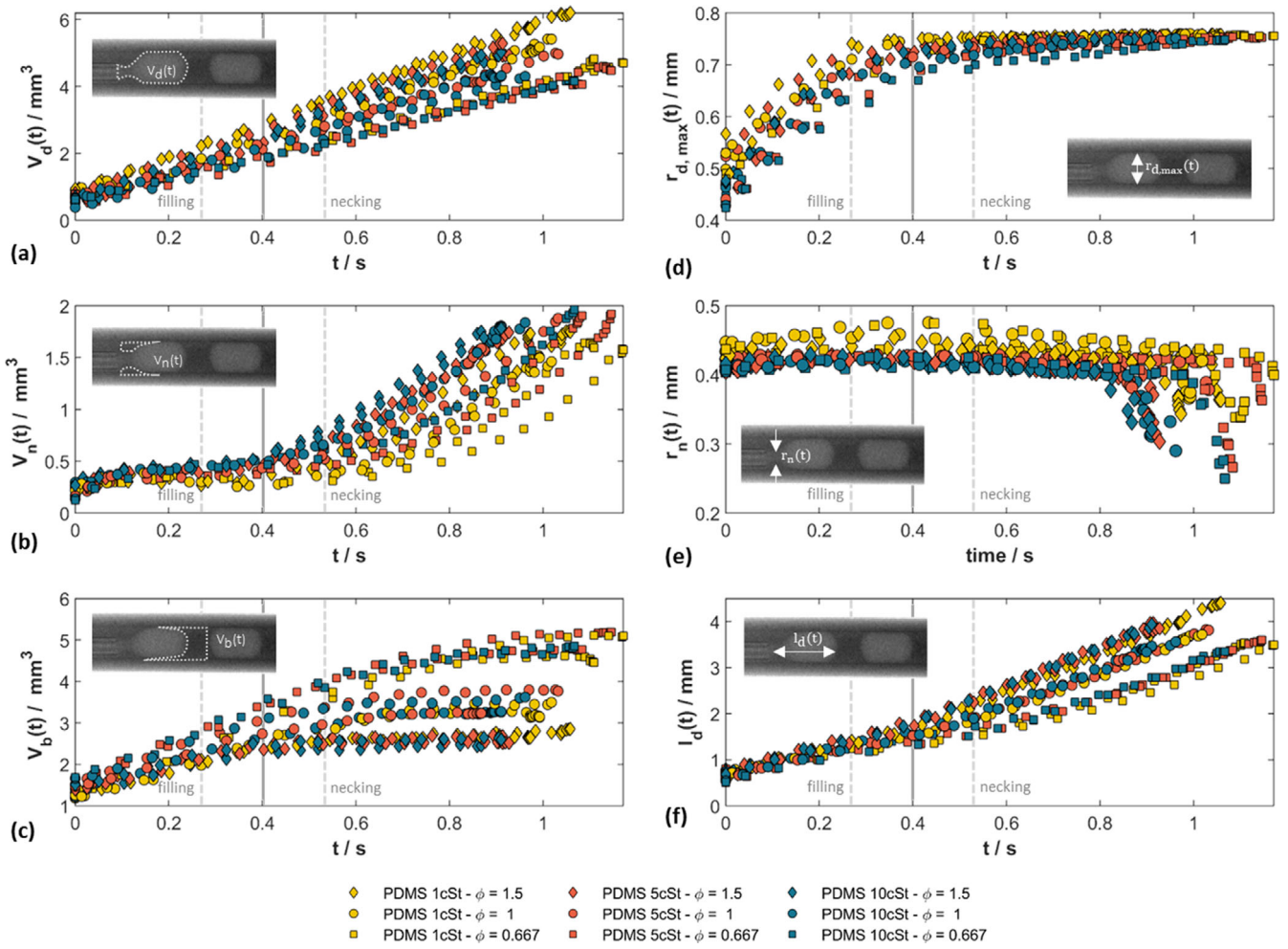

FIGURE 5 Evolution of (a) droplet volume, (b) necking volume, (c) bypassing volume, (d) maximum droplet radius, (e) minimum neck radius, and (f) droplet length over time. The vertical lines (-) and (--) mark the transition range between the filling stage and the necking stage. Droplet images are X-ray projections. The capillary diameter is 1.58 mm (measured in CT) [Color figure can be viewed at wileyonlinelibrary.com]

explained later. The vertical lines in Figure 5 mark the range of transition points with the minimum (dashed line, left), the maximum (dashed line, right), and the mean (solid line) transition point for the experiments in this work.

In the filling stage, the droplet evolves in the radial and axial direction, as can be seen from the increase of maximum droplet radius $r_{d,max}$ and droplet length l_d in Figure 5(d),(f). A higher flow rate of the dispersed phase (associated with higher ϕ) leads to a faster increase of the maximum droplet radius $r_{d,max}$ in the filling stage (Figure 5(d)). The plot also shows a slower increase in $r_{d,max}$ for higher oil viscosities (associated with higher Ca). Figure 5(e) shows the evolution of the minimum neck radius $r_n(t)$. As during the filling stage no neck has been formed $r_n(t)$ corresponds to the radius directly behind the cannula and grows slowly as the droplet increases. Thereby, $r_n(t)$ is highest for the lowest oil viscosity. For the evaluation of the continuous phase, the volume that accumulates behind the neck $V_n(t)$ and the bypassing volume $V_b(t)$ are considered separately. In the filling stage, the continuous phase can bypass the droplet easily. Therefore, the amount of bypassed volume V_b increases linearly (Figure 5(c)) according to the adjusted PDMS volume flow rate, which means inversely proportional to ϕ. At the same time, almost no volume of the continuous phase accumulates upstream the droplet, and the necking volume $V_n(t)$ remains nearly constant, regardless of ϕ or Ca, see Figure 5(b). The increasing blockage of the main channel by the emerging droplet causes the pressure in the continuous phase upstream of the droplet to increase until it reaches a maximum. This marks the end of the filling stage.

Figure 6 shows the droplet volume at the end of the filling stage (a) and the time until the end of the filling stage is reached (b). It can be seen that the filling volume V_{fill} neither depends on Ca nor ϕ, but fluctuates around a value of $V_{fill} = 2.2 \pm 0.36\,\text{mm}^3$. As this value is close to the volume of an ideal sphere $\left(V_{is} = 2.1\,\text{mm}^3\right)$ with radius $d_{is} = 1.58\,\text{mm}$ being the inner radius of the FEP tube, it is assumed that V_{fill} is a geometry dependent parameter as already stated in other work.[17,21,37] A constant value of V_{fill} means that the filling stage does not affect the resulting droplet size. The duration of the filling stage t_{fill} increases with $1/\phi$ and slightly with Ca.

In the necking stage, the pressure upstream of the droplet decreases slowly as the droplet is pushed in the downstream direction by the continuous fluid. The droplet has almost reached its maximum

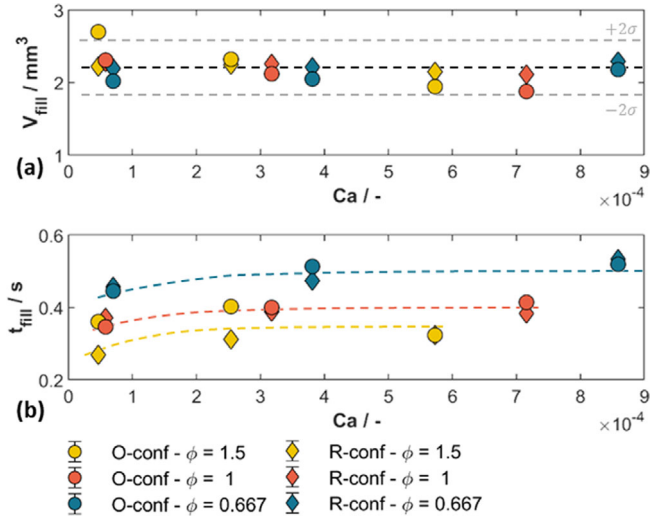

FIGURE 6 (a) Volume of the droplet at the end of the filling stage. (b) Time until the end of the filling stage is reached [Color figure can be viewed at wileyonlinelibrary.com]

radial extension, Figure 5(d), and droplet growth is mainly in the flow direction. Both effects contribute to an accelerated evolution of droplet length in the necking stage, Figure 5(f). Thereby, higher flow rate ratios ϕ lead to a faster evolution of droplet length. This means that a certain portion of the continuous phase bypasses the droplet, which was also reported by Korczyk et al.[18] Otherwise, if no continuous phase would bypass the droplet, the tip of the droplet would move forward with a velocity resulting from the total adjusted volume flow rate. However, the total volume flow rate is constant in all experiments, hence, no effect of ϕ would be visible. The blockage of the main channel in the necking stage causes a rapid increase in the necking volume $V_n(t)$. Thereby, $V_n(t)$ starts to rise sooner for a higher oil viscosity, which correlates well with the behavior of $r_{d,max}$. Additionally, the increase in $V_n(t)$ is sooner for a higher volume flow rate ratio ϕ because higher ϕ leads to sooner blockage of the main channel. Per definition, the evolution of V_b and V_n show opposite behavior. Therefore, the increase in $V_b(t)$ decelerates until the evolution of $V_b(t)$ almost stagnates as V_n increases over time. A lower volume flow rate ratio ϕ leads to later flattening of the progression of $V_b(t)$. The progressions of V_b and V_n support the observation and conclusion for the evolution of $l_d(t)$ that a certain proportion of continuous phase bypasses the emerging droplet. In the necking stage, the minimum neck radius radius $r_n(t)$ decreases slowly because the droplet is slowly pushed in the downstream direction by the continuous phase, which causes slow thinning of the neck, Figure 5(e). Eventually, the rate of neck collapse increases significantly as can be seen from the sharp decrease r_n. This finally leads to the pinch-off of the droplet.

3.3 | Investigation of droplet surface and Laplace pressure

Figure 7(a) shows the evolution of the water/oil interfacial area S_d over the droplet volume V_d. At the beginning of the droplet formation cycle, the surface evolution over volume is equal for all experimental

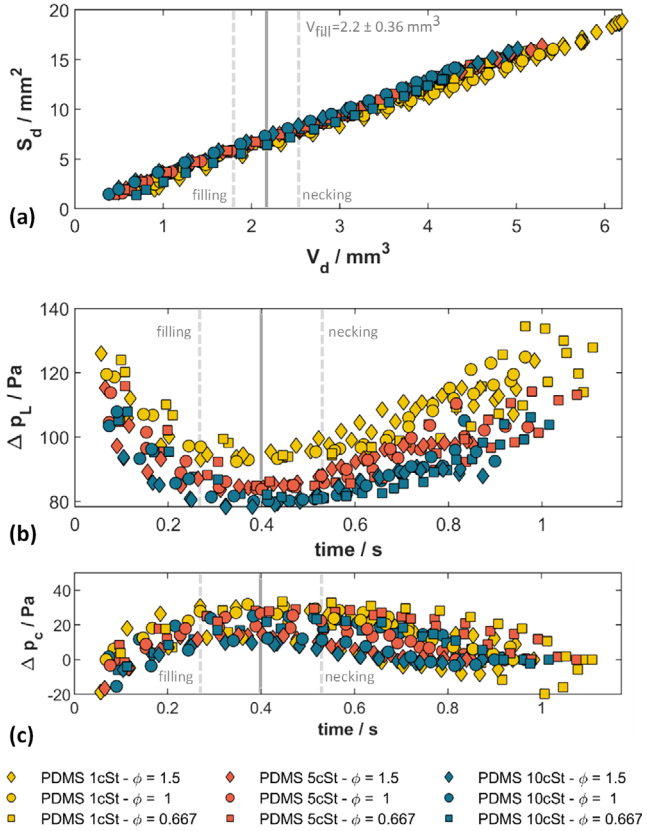

FIGURE 7 (a) Evolution of the droplet surface with droplet volume. (b) Evolution of Laplace pressure difference over time. (c) Qualitative evolution of Δp_c over time. In the necking stage, Δp_c represents the change of the pressure difference upstream and downstream of the droplet in the continuous phase [Color figure can be viewed at wileyonlinelibrary.com]

conditions tested. The droplet shape is not affected by the different flow conditions (Ca, ϕ). Therefore, it can be assumed that the surface area S_d evolves in a series of equilibrium states, as already stated by Garstecki et al.[23] In the necking stage ($V_d > 2.2 \pm 0.36\,\text{mm}^3$), S_d is slightly lower for the lowest oil viscosity tested, where the maximum droplet radius $r_{d,max}$ evolves quickest and the maximum droplet extension is reached at the end of the filling stage. Additionally, Figure 7(a) shows that droplet volumes and droplet surfaces increase to higher values for the lowest oil viscosity than for the highest oil viscosity.

The Laplace pressure Δp_L can be calculated by Equation (7)[58] and is shown in Figure 7(b).

$$\Delta p_L = \gamma \frac{dS_d}{dV_d} \tag{7}$$

In the filling stage, the Laplace pressure difference decreases according to the increase of the droplet extension in radial and axial direction. Δp_L reaches a minimum, which marks the end of the filling stage. Generally, the minimum of Δp_L is lower for higher oil viscosities, thus, higher Ca. In the necking stage, the Laplace pressure difference increases again as the droplet is pushed in the downstream direction. Δp_L reaches a local maximum closely before pinch-off. It should be

noted that the fluctuations visible for the curves PDMS 1cSt, ϕ = 0.667 result from noise magnification via derivation according to Equation (7).

Under the assumption that the shape of the cap of the droplet remains constant in the necking stage, $\frac{dS_d}{dV_d}$ in Equation (7) is solely affected by the forming neck. Therefore, under the assumption of a constant pressure p_d in the dispersed phase, the pressure difference in the continuous phase upstream and downstream of the droplet Δp_c is given by Equation (8).

$$\Delta p_c = p_d - \Delta p_L \tag{8}$$

As the pressure of the dispersed phase is not measured in this work, a constant value p_d is assumed for each condition tested. The values are chosen such that at the end of one formation cycle Δp_c equals zero. This leads to the qualitative evolution of Δp_c in the necking stage depicted in Figure 7(c). It qualitatively shows that after reaching a maximum, which marks the end of the filling stage, Δp_c decreases until pinch-off. As shown in Figure 7(c) the pressure fluctuations in the continuous phase in one droplet formation cycle are in the range of 9.7–33.4 Pa. Additionally, they are slightly stronger for lower oil viscosities (lower Ca), which confirms findings by Abate et al.[16]

3.4 | Analysis of final droplet volume $V_{d,det}$

Figure 8 shows the volume of the detached droplets $V_{d,det}$ over Ca and for the different flow rate ratios ϕ. The values given in the figure are the mean values of $V_{d,det}$. They are obtained by averaging the volume of a droplet at different times after droplet detachment. The error of image processing, represented by error bars, is calculated by the standard deviation (2σ). It is very low, which proofs reproducibility. The volumes of the detached droplets are higher as ϕ increases. For the higher capillary numbers tested, the final droplet size is nearly independent of Ca. This is what typically has been observed in the squeezing regime.[17,37,39] Additionally, $V_{d,det}$ slightly increases with decreasing Ca numbers, if Ca is low. This points to the transition from the squeezing to the leaking regime as reported by Korczyk et al.,[18] who described the same Ca-dependence of the length of the detached droplet for a cross-flow setup.

The experimental results for $V_{d,det}$ in this work are fitted to the model of Korczyk et al.[18] Therefore, Equation (5) is transformed into its volume equivalent, Equation (9), where V_{fill}, $V_{\Delta n}$, and β represent the parameters to be adjusted through the fitting. This results in $V_{fill} = 2.6135 \pm 0.31\,\mathrm{mm}^3$, $V_{\Delta n} = 1.1998 \pm 0.28\,\mathrm{mm}^3$, and $\beta = (3.0125 \pm 1.4) \cdot 10^{-5}$ (uncertainty of fitted parameters 2σ) for the tested co-flow droplet generation in the 1.58 mm capillary. The resulting curves are given in Figure 8 with solid lines.

$$V_{d,det} = V_{fill} + \phi V_{\Delta n}\left(1 + \frac{\beta}{\phi\, Ca}\right) \tag{9}$$

It should be mentioned that the calculated values V_{fill}, $V_{\Delta n}$, and β show large standard deviations due to the low number of data points.

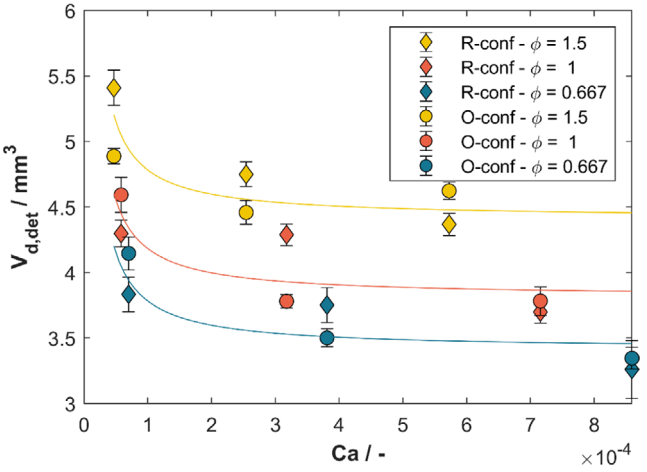

FIGURE 8 Volume of resulting droplet over capillary number and different volume flow rate ratios $\phi = \dot{V}_{dis}/\dot{V}_c$. The total flow rate is held constant at 0.5 mL min^{-1}. Solid lines result from fitting of the data to Equation (9) (Result: V_{fill} = 2.6135 ± 0.31 mm^3, $V_{\Delta n}$ = 1.1998 ± 028 mm^3, and $\beta = (3.0125 \pm 1.4) \cdot 10^{-5}$). Error bars represent standard deviations (2σ) [Color figure can be viewed at wileyonlinelibrary.com]

However, the figure shows that the model of Korczyk et al.[18] is suitable for the prediction of the qualitative behavior of droplet generation in a co-flow configuration and circular channels.

3.5 | Investigation of relative leaking strength

Korczyk et al.[18] demonstrated that the physics of droplet generation can be summarized by considering the relative leaking strength η as a function of Ca and ϕ. Here, η is the ratio of the proportion of continuous phase bypassing the forming droplet $\dot{V}_b$ and the proportion of continuous phase contributing to necking $\dot{V}_n$.[18]

$$\eta = \frac{\dot{V}_b}{\dot{V}_n} = \frac{V_{d,det} - V_{d,fill}}{\phi\, V_{\Delta n}} = \frac{\beta}{\phi\, Ca} \tag{10}$$

It can also be described in terms of $\eta = f(V_{d,det}, V_{d,fill}, \phi, V_{\Delta n})$ or by $\eta = f(\beta, \phi, Ca)$ as shown in Equation (10), where $V_{\Delta n}$ is the difference between neck volume closely before pinch-off at pinch-off time t_{po} and at the end of the filling stage t_{fill}, see Equation (11).

$$V_{\Delta n} = V_n(t_{po}) - V_n(t_{fill}) \tag{11}$$

In this work, $V_{d,det}$, $V_{d,fill}$, and $V_{\Delta n}$ can be evaluated directly using the presented tomography approach, which allows for the calculation of $\eta = f(V_{d,det}, V_{d,fill}, \phi, V_{\Delta n})$ from experimental data. The results are presented as points in Figure 9. Additionally, Figure 9 shows the calculated values for η calculated using $\eta = \frac{\beta}{\phi\, Ca}$ as solid lines for β as obtained by Korczyk et al.[18] (solid) and β obtained by fitting $V_{d,det}$ in this work (dashed). It should be pointed out that the calculated values η in the fitted master curve (dashed line) are not obtained by fitting Equation (10) to the experimental values for η (dots), but from the fit

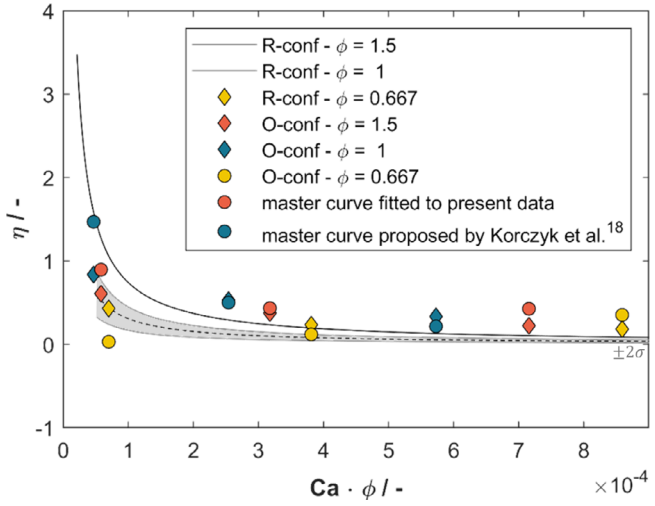

FIGURE 9 Summary of experimental results in terms of $\eta = f(V_{d,det}, V_{d,fill}, \phi, V_{\Delta n})$. Master curve proposed by Korczyk et al.[18] and master curve fitted to experimental data with $\beta = (3.0125 \pm 1.4) \cdot 10^{-5}$. The standard deviation 2σ (gray area) indicates the reliability of the fitted master curve [Color figure can be viewed at wileyonlinelibrary.com]

of Equation (9) to the experimental values of $V_{d,det}$, as described in the previous section.

As can be seen from the experimental data in Figure 9 (dots), the relative leaking strength is nearly independent of the product $Ca \cdot \phi$ for $Ca \cdot \phi > 1 \cdot 10^{-4}$ with slightly decreasing leaking strengths η for increasing values of $Ca \cdot \phi$. For lower $Ca \cdot \phi$ ($Ca \cdot \phi < 1 \cdot 10^{-4}$) η increases as $Ca \cdot \phi$ decreases. This suggests that the droplet generation regime transitions from the squeezing regime to the leaking regime as the product $Ca \cdot \phi$ decreases. This qualitative behavior is captured by both master curves given in the figure. However, the master curve obtained from the fitting of β to own experimental data better represents the experimental values for η at the transition from squeezing to leaking. Korczyk et al.[18] define the transition from the squeezing regime to the leaking regime for $\eta = 1$ at $Ca \cdot \phi = \beta = 7.4 \cdot 10^{-5} \pm 0.3 \cdot 10^{-5}$.[11] In this work, the transition takes place at a lower value $Ca \cdot \phi$ ($Ca \cdot \phi = \beta = (3.0125 \pm 1.4) \cdot 10^{-5}$). The high value of the standard deviation in this work results from the small number of data points. However, the lower value $Ca \cdot \phi$ compared to the value of Korczyk et al.[18] suggests that in circular channels leaking is less relevant at the same $Ca \cdot \phi$ compared to rectangular channels and that the transition from squeezing to leaking takes place at lower $Ca \cdot \phi$.

The relative leaking strength can be used to calculate the ratio between the fluid bypassing the droplet and the total volume flow rate of the continuous phase by using Equation (12).

$$\frac{\dot{V}_b}{\dot{V}_c} = \frac{1}{\frac{1}{\eta} + 1} \tag{12}$$

From the master curve fitted to own experimental data in the range $4.7 \cdot 10^{-5} < Ca \cdot \phi < 8.6 \cdot 10^{-4}$ the proportion of the continuous phase that bypasses the emerging droplet is $37\% > \frac{\dot{V}_b}{\dot{V}_c} > 3\%$. As described previously, leaking is stronger for lower values of $Ca \cdot \phi$. Yao et al.[42] reported the ratio $\frac{\dot{V}_b}{\dot{V}_c}$ for a rectangular channel and complete wetting in the range $1.5 \cdot 10^{-4} < Ca \cdot \phi < 6.1 \cdot 10^{-4}$. The portion of bypassing liquid was found to be approximately in the range $25\% > \frac{\dot{V}_b}{\dot{V}_c} > 11\%$ for the emerging droplet.[42] In the same range of $Ca \cdot \phi$, the master curve fitted to own experimental data shows $17\% > Ca \cdot \phi > 5\%$ for the emerging droplet. The portion of continuous phase bypassing the droplet is lower by approximately a factor of two for the circular channel tested in this work compared to the rectangular channel tested by Yao et al.,[42] which supports the thesis that leaking is less relevant for circular channels. In contrast to circular channels, the emerging droplet does not cover the cross-sectional area of a rectangular channel uniformly. As the emerging droplet aims to minimize energy via surface minimization the corners of a rectangular channel remain uncovered by the dispersed phase. The portion of the cross-sectional area for the flow of bypassing liquid is larger compared to circular tubes, which results in lower flow resistance. Therefore, the importance of leaking is lower in circular channels than in rectangular channels, which is proved in this work.

4 | SUMMARY AND OUTLOOK

Micro-computed tomography was applied for the investigation of highly periodic droplet formation in a co-flow needle-in-capillary arrangement ($d_i \approx 1.58$ *mm*) at low capillary numbers. Water droplets were generated in the co-flow configuration with silicone oil as the continuous phase. A scanning protocol followed by a postprocessing procedure, the multiple-select method, was developed. By applying the multiple-select method the temporal resolution for X-ray-based micro-computed tomography was enhanced to 0.05 s. The time-resolved 3D data generated using the multiple-select method allowed for the determination of different droplet quantities (length, diameter, surface, volume, Laplace pressure difference).

Droplet surfaces were visualized at different stages of formation and different experimental conditions (capillary number range $4.7 \cdot 10^{-5} - 8.6 \cdot 10^{-4}$, volume flow rate ratio of dispersed to continuous phase from 0.667 to 1.5). The evolution of the filling and necking stage was investigated in more detail. One important finding is that the volume at the end of the filling stage is independent of the capillary number and flow rate ratio ($V_{fill} = 2.2 \pm 0.36\,\mathrm{mm}^3$). Therefore, the final droplet size is only affected by the underlying physics of the necking stage.

The analysis of the effect of capillary number and volume flow rate ratio on the volume of the resulting droplet showed that the final droplet increases with flow rate ratio and decreases with the capillary number. This suggests that the leaking regime as presented by Korczyk et al.[18] also applies for the co-flow configuration used in this work.

A comparison of data presented by Yao et al.[42] to own experimental results revealed that the proportion of continuous phase that bypasses the droplet is approximately reduced by a factor of two,

which means that leaking is less relevant in circular channels than in rectangular channels. Additionally, the transition from squeezing to leaking was found to be at lower values $Ca \cdot \phi$ for circular channels ($Ca \cdot \phi = (3.0125 \pm 1.4) \cdot 10^{-5}$) than for rectangular channels ($Ca \cdot \phi = (7.4 \pm 0.3) \cdot 10^{-5}$) as found by Korczyk et al.[18]

The analysis of the evolution of droplet surface over droplet volume supports the assumption that droplet evolves in a series of equilibrium states. The amplitude of pressure fluctuation in the continuous phase upstream of the emerging droplet was found to be in the range of 9.7–33.4 Pa. It was found that the fluctuations decrease as the capillary number increases, which is supported by findings in the literature.[16]

With this work, we prove the suitability of the presented methodology for the time-resolved 3D investigation of droplet formation and demonstrated how 3D quantities help to understand the underlying physics. The presented methodology can be applied to the investigation of diverse highly periodic processes and is not limited to circular channels or liquid–liquid flow, but a new training of CNN might be necessary. Interesting insights are expected from the extension of recent investigations to gas/liquid flow, where the compressibility of the gas additionally affects bubble formation, and droplet or bubble generation in rectangular channels, where the focus will be on the corner flow. All experimental results obtained with micro-computed tomography can be used for accurate validation of 3D numerical simulations performed in a computational domain obtained from the scans. The combination of 3D numerical simulation and 3D tomographic imaging will give further insights into the 3D flow situation during liquid/liquid droplet formation.

NOTATION

LATIN SYMBOLS

A_{cross}	area of cross-section (m^2)
Ca	capillary number
d	diameter (m)
f	frequency (s^{-1})
K	curvature (m^{-1})
l	length (m)
O	original run
p	absolute pressure (Pa)
Δp_c	pressure difference in the continuous phase (Pa)
Δp_L	Laplace pressure difference (Pa)
r	radius (m)
R	reproduction run
R_b	flow resistance (Pa s m^{-3})
S	surface (m^2)
t	time (s)
T_a	ambient temperature (K)
v	mean velocity (m s^{-1})
V	volume (m^3)
$\dot{V}$	volume flow rate (m^3 s^{-1})
w_c	channel width (m)

GREEK LETTERS

α	geometry constant
β	constant
γ	interfacial tension (N m^{-1})
η	relative leaking strength
η_c	dynamic viscosity (Pa s)
θ	angular position (°)
ρ	density (kg m^{-3})
σ	standard deviation (diverse)
ϕ	volume flow rate ratio

SUBSCRIPTS

a	amplitude
b	bypass
B	rear of droplet
c	continuous phase
d	droplet
dis	dispersed phase
det	detached droplet
fill	filling stage
F	front of droplet
i	inner
is	ideal sphere
max	maximum
n	necking
Δn	difference over necking stage
o	outer
po	pinch-off
x	placeholder
*	dimensionless

ACKNOWLEDGMENTS

The authors would like to thank the German Research Foundation (DFG, grant number INST 212/397-1) for granting the Bruker Skyscan 1275. We acknowledge financial support by German Research Foundation (DFG) and TU Dortmund University within the funding programme Open Access Publishing. Additionally, we would like to thank RJL Micro & Analytic, Karlsdorf-Neuthard, Germany, for technical support and training. Furthermore, we would like to acknowledge, G. Schaldach (Laboratory of Solids Process Engineering, TU Dortmund University, Germany) and C. Schrömges (Laboratory of Equipment Design, TU Dortmund University, Germany) for technical advice. Finally, we thank J. Herath (Laboratory of Equipment Design, TU Dortmund University, Germany) for assistance in performing the experiments. Open access funding enabled and organized by Projekt DEAL.

ORCID

Julia Schuler https://orcid.org/0000-0002-0848-0219

REFERENCES

1. Günther A, Jensen KF. Multiphase microfluidics: from flow characteristics to chemical and materials synthesis. *Lab Chip*. 2006;6:1487-1503. https://doi.org/10.1039/b609851g.
2. Chan EM, Alivisatos AP, Mathies RA. High-temperature microfluidic synthesis of CdSe nanocrystals in nanoliter droplets. *J Am Chem Soc*. 2005;127:13854-13861. https://doi.org/10.1021/ja051381p.
3. Song H, Chen DL, Ismagilov RF. Reactions in droplets in microfluidic channels. *Angew Chem Int Ed*. 2006;45:7336-7356. https://doi.org/10.1002/anie.200601554.
4. Yen BKH, Günther A, Schmidt MA, Jensen KF, Bawendi MG. A microfabricated gas-liquid segmented flow reactor for high-temperature synthesis: the case of CdSe quantum dots. *Angew Chem*. 2005;117:5583-5587. https://doi.org/10.1002/ange.200500792.
5. Zhang H, Tumarkin E, Peerani R, et al. Microfluidic production of biopolymer microcapsules with controlled morphology. *J Am Chem Soc*. 2006;128:12205-12210. https://doi.org/10.1021/ja0635682.
6. Bui M-PN, Li CA, Han KN, Choo J, Lee EK, Seong GH. Enzyme kinetic measurements using a droplet-based microfluidic system with a concentration gradient. *Anal Chem*. 2011;83:1603-1608. https://doi.org/10.1021/ac102472a.
7. Krieger W, Hörbelt M, Schuster S, Hennekes J, Kockmann N. Kinetic study of Leuco-indigo carmine oxidation and investigation of Taylor and dean flow superposition in a coiled flow inverter. *Chem Eng Technol*. 2019;42:2052-2060. https://doi.org/10.1002/ceat.201800753.
8. Ciceri D, Perera JM, Stevens GW. The use of microfluidic devices in solvent extraction. *J Chem Technol Biotechnol*. 2014;89:771-786. https://doi.org/10.1002/jctb.4318.
9. Launiere CA, Gelis AV. High precision droplet-based microfluidic determination of americium(III) and lanthanide(III) solvent extraction separation kinetics. *Ind Eng Chem Res*. 2016;55:2272-2276. https://doi.org/10.1021/acs.iecr.5b04691.
10. Ferreira J, Castro F, Rocha F, Kuhn S. Protein crystallization in a droplet-based microfluidic device: hydrodynamic analysis and study of the phase behaviour. *Chem Eng Sci*. 2018;191:232-244. https://doi.org/10.1016/j.ces.2018.06.066.
11. Ferreira J, Castro F, Kuhn S, Rocha F. Controlled protein crystal nucleation in microreactors: the effect of the droplet volume versus high supersaturation ratios. *CrstEngComm*. 2020;22:4692-4701. https://doi.org/10.1039/D0CE00517G.
12. DeMello AJ. Control and detection of chemical reactions in microfluidic systems. *Nature*. 2006;442:394-402. https://doi.org/10.1038/nature05062.
13. Sohrabi S, kassir N, Keshavarz Moraveji M. Droplet microfluidics: fundamentals and its advanced applications. *RSC Adv*. 2020;10:27560-27574. https://doi.org/10.1039/D0RA04566G.
14. Feng H, Zheng T, Li M, et al. Droplet-based microfluidics systems in biomedical applications. *Electrophoresis*. 2019;40:1580-1590. https://doi.org/10.1002/elps.201900047.
15. Thorsen T, Roberts RW, Arnold FH, Quake SR. Dynamic pattern formation in a vesicle-generating microfluidic device. *Phys Rev Lett*. 2001;86:4163-4166. https://doi.org/10.1103/PhysRevLett.86.4163.
16. Abate AR, Mary P, van Steijn V, Weitz DA. Experimental validation of plugging during drop formation in a T-junction. *Lab Chip*. 2012;12:1516-1521. https://doi.org/10.1039/c2lc21263c.
17. Garstecki P, Fuerstman MJ, Stone HA, Whitesides GM. Formation of droplets and bubbles in a microfluidic T-junction-scaling and mechanism of break-up. *Lab Chip*. 2006;6:437-446. https://doi.org/10.1039/B510841A.
18. Korczyk PM, van Steijn V, Blonski S, Zaremba D, Beattie DA, Garstecki P. Accounting for corner flow unifies the understanding of droplet formation in microfluidic channels. *Nat Commun*. 2019;10:2528. https://doi.org/10.1038/s41467-019-10505-5.
19. van Loo S, Stoukatch S, Kraft M, Gilet T. Droplet formation by squeezing in a microfluidic cross-junction. *Microfluid Nanofluid*. 2016;20:1-12. https://doi.org/10.1007/s10404-016-1807-1.
20. van Steijn V, Kleijn CR, Kreutzer MT. Flows around confined bubbles and their importance in triggering pinch-off. *Phys Rev Lett*. 2009;103:214501. https://doi.org/10.1103/PhysRevLett.103.214501.
21. van Steijn V, Kleijn CR, Kreutzer MT. Predictive model for the size of bubbles and droplets created in microfluidic T-junctions. *Lab Chip*. 2010;10:2513-2518. https://doi.org/10.1039/c002625e.
22. Chen X, Glawdel T, Cui N, Ren CL. Model of droplet generation in flow focusing generators operating in the squeezing regime. *Microfluid. Nanofluid.* 2015;18:1341-1353. https://doi.org/10.1007/s10404-014-1533-5.
23. Garstecki P, Stone HA, Whitesides GM. Mechanism for flow-rate controlled breakup in confined geometries: a route to monodisperse emulsions. *Phys Rev Lett*. 2005;94:164501. https://doi.org/10.1103/PhysRevLett.94.164501.
24. Lee W, Walker LM, Anna SL. Role of geometry and fluid properties in droplet and thread formation processes in planar flow focusing. *Phys Fluids*. 2009;21:32103. https://doi.org/10.1063/1.3081407.
25. Jensen MJ, Stone HA, Bruus H. A numerical study of two-phase stokes flow in an axisymmetric flow-focusing device. *Phys Fluids*. 2006;18:77103. https://doi.org/10.1063/1.2214461.
26. Jeong WJ, Kim JY, Choo J, et al. Continuous fabrication of biocatalyst immobilized microparticles using photopolymerization and immiscible liquids in microfluidic systems. *Langmuir*. 2005;21:3738-3741. https://doi.org/10.1021/la050105l.
27. Kim J-W, Utada AS, Fernández-Nieves A, Hu Z, Weitz DA. Fabrication of monodisperse gel shells and functional microgels in microfluidic devices. *Angew Chem Int Ed*. 2007;46:1819-1822. https://doi.org/10.1002/anie.200604206.
28. Xu K, Tostado CP, Xu J-H, Lu Y-C, Luo G-S. Direct measurement of the differential pressure during drop formation in a co-flow microfluidic device. *Lab Chip*. 2014;14:1357-1366. https://doi.org/10.1039/c3lc51222c.
29. Nisisako T, Torii T, Takahashi T, Takizawa Y. Synthesis of Monodisperse bicolored Janus particles with electrical anisotropy using a microfluidic co-flow system. *Adv Mater*. 2006;18:1152-1156. https://doi.org/10.1002/adma.200502431.
30. Biswas KG, Patra R, Das G, Ray S, Basu JK. Effect of flow orientation on liquid–liquid slug flow in a capillary tube. *Chem Eng J*. 2015;262:436-446. https://doi.org/10.1016/j.cej.2014.09.122.
31. Kashid MN, Rivas DF, Agar DW, Turek S. On the hydrodynamics of liquid-liquid slug flow capillary microreactors. *Asia-Pac J Chem Eng*. 2008;3:151-160. https://doi.org/10.1002/apj.127.
32. Kashid M, Kiwi-Minsker L. Quantitative prediction of flow patterns in liquid–liquid flow in micro-capillaries. *Chem Eng Process Process Intensif*. 2011;50:972-978. https://doi.org/10.1016/j.cep.2011.07.003.
33. Kashid MN, Agar DW. Hydrodynamics of liquid–liquid slug flow capillary microreactor: flow regimes, slug size and pressure drop. *Chem Eng J*. 2007;131:1-13. https://doi.org/10.1016/j.cej.2006.11.020.
34. Krieger W, Bayraktar E, Mierka O, et al. Arduino-based slider setup for gas–liquid mass transfer investigations: experiments and CFD simulations. *AIChE J*. 2020;66:1-13. https://doi.org/10.1002/aic.16953.
35. Lee W, Kwon D, Choi W, Jung GY, Jeon S. 3D-printed microfluidic device for the detection of pathogenic bacteria using size-based separation in helical channel with trapezoid cross-section. *Sci Rep*. 2015;5:7717. https://doi.org/10.1038/srep07717.
36. Wu L, Guan G, Hou HW, Bhagat AAS, Han J. Separation of leukocytes from blood using spiral channel with trapezoid cross-section. *Anal Chem*. 2012;84:9324-9331. https://doi.org/10.1021/ac302085y.

37. Anna SL. Droplets and bubbles in microfluidic devices. *Annu Rev Fluid Mech*. 2016;48:285-309. https://doi.org/10.1146/annurev-fluid-122414-034425.
38. Glawdel T, Elbuken C, Ren CL. Droplet formation in microfluidic T-junction generators operating in the transitional regime. I. Experimental observations. *Phys Rev E*. 2012;85:16322. https://doi.org/10.1103/PhysRevE.85.016322.
39. Christopher GF, Anna SL. Microfluidic methods for generating continuous droplet streams. *J Phys D Appl Phys*. 2007;40:R319-R336. https://doi.org/10.1088/0022-3727/40/19/R01.
40. van Steijn V, Kreutzer MT, Kleijn CR. μ -PIV study of the formation of segmented flow in microfluidic T-junctions. *Chem Eng Sci*. 2007;62:7505-7514. https://doi.org/10.1016/j.ces.2007.08.068.
41. Yao C, Dong Z, Zhang Y, Mi Y, Zhao Y, Chen G. On the leakage flow around gas bubbles in slug flow in a microchannel. *AIChE J*. 2015;61:3964-3972. https://doi.org/10.1002/aic.14895.
42. Yao C, Liu Y, Xu C, Zhao S, Chen G. Formation of liquid-liquid slug flow in a microfluidic T-junction: effects of fluid properties and leakage flow. *AIChE J*. 2018;64:346-357. https://doi.org/10.1002/aic.15889.
43. Musterd M, van Steijn V, Kleijn CR, Kreutzer MT. Calculating the volume of elongated bubbles and droplets in microchannels from a top view image. *RSC Adv*. 2015;5:16042-16049. https://doi.org/10.1039/c4ra15163a.
44. Schuler J, Kockmann N. Micro-computed tomography for the investigation of stationary liquid–liquid and liquid–gas interfaces in capillaries. *AIChE J*. 2019;66:1-12. https://doi.org/10.1002/aic.16890.
45. Aferka S, Viva A, Brunazzi E, Marchot P, Crine M, Toye D. Tomographic measurement of liquid hold up and effective interfacial area distributions in a column packed with high performance structured packings. *Chem Eng Sci*. 2011;66:3413-3422. https://doi.org/10.1016/j.ces.2011.01.022.
46. Aferka S, Marchot P, Crine M, Toye D. Interfacial area measurement in a catalytic distillation packing using high energy X-ray CT. *Chem Eng Sci*. 2010;65:511-516. https://doi.org/10.1016/j.ces.2009.05.048.
47. Bieberle M, Barthel F, Hampel U. Ultrafast X-ray computed tomography for the analysis of gas–solid fluidized beds. *Chem Eng J*. 2012;189-190:356-363. https://doi.org/10.1016/j.cej.2012.02.028.
48. Schmit C E, Eldridge RB. Investigation of X-ray imaging of vapor–liquid contactors. 1. Studies involving stationary objects and a simple flow system. *Chem Eng Sci*. 2004;59:1255-1266. https://doi.org/10.1016/j.ces.2003.09.045.
49. Janzen A, Steube J, Aferka S, et al. Investigation of liquid flow morphology inside a structured packing using X-ray tomography. *Chem Eng Sci*. 2013;102:451-460. https://doi.org/10.1016/j.ces.2013.08.035.
50. Mudde RF. Bubbles in a fluidized bed: a fast X-ray scanner. *AIChE J*. 2011;57:2684-2690. https://doi.org/10.1002/aic.12469.
51. Toye D, Marchot P, Crine M, Pelsser A-M, L'Homme G. Local measurements of void fraction and liquid holdup in packed columns using X-ray computed tomography. *Chem Eng Process Process Intensif*. 1998;37:511-520. https://doi.org/10.1016/S0255-2701(98)00058-0.
52. Bruker Corporation. SkyScan 1275; 2016. https://www.bruker.com/products/microtomography/micro-ct-for-sample-scanning/skyscan-1275/technical-details.html. Accessed February 5, 2019.
53. Liebling M, Forouhar AS, Gharib M, Fraser SE, Dickinson ME. Four-dimensional cardiac imaging in living embryos via postacquisition synchronization of nongated slice sequences. *J Biomed Opt*. 2005;10:54001. https://doi.org/10.1117/1.2061567.
54. Liu A, Wang R, Thornburg KL, Rugonyi S. Efficient postacquisition synchronization of 4-D nongated cardiac images obtained from optical coherence tomography: application to 4-D reconstruction of the chick embryonic heart. *J Biomed Opt*. 2009;14:44020. https://doi.org/10.1117/1.3184462.
55. Mickoleit M, Schmid B, Weber M, et al. High-resolution reconstruction of the beating zebrafish heart. *Nat Methods*. 2014;11:919-922. https://doi.org/10.1038/nmeth.3037.
56. Simonyan K, Zisserman A. Very deep convolutional networks for large-scale image recognition; 2014. http://arxiv.org/pdf/1409.1556v6.
57. The MathWorks, Inc. Pretrained Deep Neural Networks https://www.mathworks.com/help/deeplearning/ug/pretrained-convolutional-neural-networks.html. Accessed August 17, 2020.
58. Blunt MJ. *Multiphase flow in permeable media: a pore-scale perspective*. Cambridge: Cambridge University Press; 2017.

SUPPORTING INFORMATION

Additional supporting information may be found online in the Supporting Information section at the end of this article.

How to cite this article: Schuler J, Neuendorf LM, Petersen K, Kockmann N. Micro-computed tomography for the 3D time-resolved investigation of monodisperse droplet generation in a co-flow setup. *AIChE J*. 2021;67:e17111. https://doi.org/10.1002/aic.17111